



# Aerosol additive manufacturing of multi-component supraparticles for Fenton reaction-assisted multi-modal anticancer treatment

Sungjae Park<sup>a,1</sup>, Kishwor Poudel<sup>b,c,1</sup>, Jiseok Lim<sup>d,1</sup>, Jaeho Oh<sup>a</sup>, Sae Kwang Ku<sup>e</sup>,  
Jungho Hwang<sup>a,\*</sup>, Jong Oh Kim<sup>b,\*</sup>, Jeong Hoon Byeon<sup>d,\*</sup>

<sup>a</sup> School of Mechanical Engineering, Yonsei University, Seoul 03722, Republic of Korea

<sup>b</sup> College of Pharmacy, Yeungnam University, Gyeongsan 38541, Republic of Korea

<sup>c</sup> Wellman Center for Photomedicine, Department of Dermatology, Meassachusetts General Hospital, Harvard Medical School, MA 02114, United States

<sup>d</sup> School of Mechanical Engineering, Yeungnam University, Gyeongsan 38541, Republic of Korea

<sup>e</sup> College of Korean Medicine, Daegu Haany University, Gyeongsan 38610 Republic of Korea

## ARTICLE INFO

### Keywords:

Aerosol additive manufacturing

Spontaneous assembly

Multi-component supraparticles

Single-pass gas flow

Chemo-chemodynamic-photothermal-

immuno combination therapeutics

## ABSTRACT

Nanoscale supraparticles have attracted considerable interest in cancer therapeutics and diagnostics because of the affordable structures that can be assembled for a stimulus response and the loading of active compounds for combinatorial theranostics. These nanostructures are usually constructed by balancing interparticle forces between colloidal particles during thermodynamics-controlled growth. On the other hand, there are no relevant studies for assembling cancer theranostic supraparticles in an aerosol state, even though nanoparticles in that state have three orders of magnitude greater diffusional behavior for thermal collision between the particles compared to those in the aqueous state, as well as the limited numbers in separation and purification steps are required in aerosol processing. Aerosol additive manufacturing is designed using electrically operable devices as a digitizable platform for the spontaneous assembly of multi-component supraparticles in a continuous medium, which does not require special reaction conditions and complex controls for the desired assembly. Aggregates from electrostatic interactions between the oppositely charged Fe (Zn or Fe-Zn) and Cu constituent particles were inserted within 1-hexanethiol-docetaxel (DTX)-bovine serum albumin (BSA) mixture droplets for photo-induced thiolation of the outermost Cu particles and subsequent co-aggregation with DTX-BSA to form Fe(Zn or Fe-Zn)CuS@DTX-BSA supraparticles in a single-pass gas flow. The resulting supraparticles were used to examine the combinatorial anticancer effects in both *in vitro* and *in vivo* models, and anti-programmed death-ligand 1 antibodies were added to validate chemo-chemodynamic-photothermal-immuno combination therapeutics with no systemic toxicity.

## 1. Introduction

Owing to the tunable size, surface chemistry, and composition of cancer cell interactions, metallic nanoparticle-mediated cancer treatments have the potential to derive optimized cancer therapies with minimal side effects [1]. Recently, to accelerate the translation of the nanoparticle-mediated strategies, cancer treatments facilitated by the Fenton (by Fe) or Fenton-like (by Cu, Mn, Co, Ti, V, Pd, Ag, Mo, Ru, W, Ce, or Zn) reaction using metallic nanoparticles generating cytotoxic reactive oxygen species (ROS), so-called chemodynamic therapy (CDT), has been studied extensively because of minimal invasiveness and

spatiotemporal tumor selectivity [2–4]. These studies led to the use of multiple metallic elements to secure all-in-one modalities (photodynamic, photothermal, and magnetothermal) to enhance the efficacy of CDT because multi-metallic nanoparticles allow coupling effects among constituent metals in a closer manner [5–8]. However, the use of multi-metallic nanoparticles has a critical issue in the process complexity of hydrothermal nanoparticle preparation from diverse reduction potentials of different metallic precursors that generate difficulties in controlling the growth kinetics and structure of nanoparticles, resulting in a significant increase in the total cost of cancer treatments [9–11]. Moreover, hydrothermal sample-by-sample approaches to prepare

\* Corresponding authors.

E-mail addresses: [hwangjh@yonsei.ac.kr](mailto:hwangjh@yonsei.ac.kr) (J. Hwang), [jongohkim@yu.ac.kr](mailto:jongohkim@yu.ac.kr) (J.O. Kim), [postjb@yu.ac.kr](mailto:postjb@yu.ac.kr) (J.H. Byeon).

<sup>1</sup> These authors contributed equally to this work.

optimal multi-metallic nanoparticles may not be affordable to a high-throughput design and synthesis toward digitizable, intelligent, and autonomous platform for smart anticancer therapies [12–15].

Additive manufacturing (AM) has recently been introduced as an electrically operable, flexible, customizable process for constructing composite particles with tailored composition and morphology through spray aggregation of colloidal dispersions [16]. On the other hand, most of the AM has been used frequently for the customized production of electronic materials, batteries, and fine polymeric structures thus far [17–19]. In terms of biomedical engineering, AM has been used to prepare microfluidic devices for analytical and assembly purposes of biological objects [20–22]. Although AM was used to build implantable devices for controlled drug release [23], there are no directly relevant studies on the preparation of anticancer nanomaterials using AM as an active dispenser, despite the recent considerable advances of AM in the era of Industry 4.0 [24].

Co-aggregation governed by a thermodynamic motion of individual nanoparticles can spontaneously form larger defined structures, also called supraparticles [25]. Similar to a multi-layered structure from the layer-by-layer assembly, multi-component supraparticles consisting of different spherical elements can be constructed rapidly by controlling the thermodynamic conditions where individual elements (building blocks) of the supraparticles tend to gather spherically as a complex precipitate to reduce surface energy within the thermodynamics (diffusion)-controlled growth regime [26]. Co-aggregation of organic molecules as self-assembly was recently used for high-throughput design of drug nanoparticles [27] while co-aggregation between organic and inorganic molecules formed multi-component supraparticles for enhanced anticancer therapies [28,29]. The characteristic surface roughness of supraparticles allows enhanced uptake for selective intracellular release of active compounds with exceptional biocompatibility and stability [30–33]. Multi-metallic supraparticles were also designed and prepared through a spontaneous co-aggregation to secure multimodality for enhanced ROS generation *in vivo* [34]. Although a previous study relevant to AM even adopted co-aggregation as the main driver to build microscale composite supraparticles [16], it is still necessary to examine the possibility of assembling nanoscale multi-component supraparticles as nanomedicines using AM for use in anticancer therapy.

Nanoparticles in the aerosol state can have three orders of magnitude greater thermal diffusion than those in the aqueous state that can theoretically facilitate a rapid spontaneous assembly of supraparticles. The stronger diffusional behavior of aerosol nanoparticles derived transformation into aggregates, even in a single-pass gas flow [35]. Motivated by this background, an aerosol AM (AAM) system was developed and constructed to assemble nanoscale multi-component supraparticles in an electrically operable, modular, single-pass, continuous configuration. Aerosol co-aggregation between the metallic aggregates (Fe–Cu, Zn–Cu, or Fe–Zn–Cu) and mixture droplets (1-hexanethiol (thiol as a –SH source to bind photon attacked metal surface) [36], docetaxel (DTX as chemodrug for supporting the Fenton/Fenton-like reaction with increased H<sub>2</sub>O<sub>2</sub> levels) [37], and bovine serum albumin (BSA as stabilizing and targeting moiety with negligible cytotoxicity) [38–40]) induced spontaneous formation of the multi-component supraparticles (FeCuS@DTX-BSA, ZnCuS@DTX-BSA, or FeZnCuS@DTX-BSA exhibiting modular coordination) by passing through a heated photoionization flow reactor, as shown in Fig. 1. In particular, the first and second stages of a tandem electrical discharge produced Fe (or Zn, Fe–Zn) and Cu nanoparticles in the presence of positive and negative gas ions, respectively. Electrostatic interaction between the positively charged Fe (or Zn, Fe–Zn) and negatively charged Cu particles (several-nanometer-sized) assembled Fe (or Zn, FeZn)Cu aggregates in the presence of nitrogen gas flow. The aggregate-laden flow passed over the nozzle of a collision-type atomizer, where the aggregates were inserted into the mixture droplets to set multi-component precursors for their co-aggregation. These precursors were then passed

through heated photoionization (6.2 eV photon energy) flow reactor for on-particle photochemistry [41] to derive CuS and extract solvent for overlaying DTX and BSA on the metallic aggregates, resulting in the formation of FeCuS (or ZnCuS, FeZnCuS)@DTX-BSA supraparticles. Fe and Zn were selected for the Fenton and Fenton-like reactions ( $\text{Fe}^{2+} + \text{H}_2\text{O}_2 \rightarrow \text{Fe}^{3+} + \bullet\text{OH} + \text{OH}^-$  and  $\text{Zn}^{2+} + \text{H}_2\text{O}_2 \rightarrow \text{Zn}^{3+} + \bullet\text{OH} + \text{OH}^-$ ) with H<sub>2</sub>O<sub>2</sub> in a tumor microenvironment, respectively [42]. The CuS component was exploited by considering its advantageous properties regarding light-to-heat conversion, Fenton-like reactivity with H<sub>2</sub>O<sub>2</sub> to generate  $\bullet\text{OH}$ , reduction of excess glutathione (GSH) in the tumor microenvironment to increase  $\bullet\text{OH}$  generation, biodegradability and biocompatibility, catalytic capability over a wider pH range, and cost-effectiveness [43–48]. In particular, the photothermal activity of CuS can improve the efficacy of the Fenton and Fenton-like CDT from the acceleration of  $\bullet\text{OH}$  generation because of the heat-induced production of intracellular H<sub>2</sub>O<sub>2</sub>. The heat can also accelerate the release of metal ions and GSH consumption for the Fenton and Fenton-like reaction that compromises the limitations of heat shock protein modification making cancer cells resistant to apoptosis from heat [49–52].

The resulting supraparticles from the flow reactor were collected on hydrophobic substrates for convenient detachment and analyses of their physicochemical (size distribution, morphology, composition, surface chemistry, and light absorption) properties and *in vitro* (cytotoxicity, ROS generation, and apoptosis, including photothermal activity and DTX release) and *in vivo* (biodistribution, bodyweight monitoring, significant organ histopathology, immunohistochemistry, cellular proliferation, and angiogenesis in the absence and presence of near-infrared (NIR) irradiation) anticancer performance. For the *in vivo* anticancer study, as an immune-checkpoint blocker (ICB), an anti-programmed death-ligand 1 antibody (aPL) was also incorporated with FeZnCuS@DTX-BSA supraparticles to boost the immune responses for a chemo–chemodynamic–photothermal–immuno combination therapy (Fig. S1), which was specifically identified by immunohistochemical analysis of the markers for immunogenic cell death (ICD with high mobility binding box 1 (HMGB1 as activation of innate immunity) and calreticulin (CRT as a pro-phagocytic marker in tumor mass) expression) and infiltration of effector T cells because ICD is one of the avenues to stimulate the tumor immunity that can be induced synergistically through chemo–, chemodynamic, and photothermal therapies along with their individual effects [53,54].

## 2. Experimental

### 2.1. Supraparticle assembly and characterization

Fe (Zn or Fe–Zn)–Cu aggregates from electrical discharges (3 kV, 1 kHz) with bipolar gas ions (carbon brush ionizers) were formed through ablation-condensation and subsequent electrostatic interaction between oppositely charged individual particles (Fe, Zn, or Cu) under nitrogen gas flow (2 L/min). The gaseous ions from the carbon brush ionizers with high concentrations ( $>10^6$  ions/cm<sup>3</sup>) were injected into the electrical discharge device to increase the discharge coefficient for stable particle supply as introduced in a previous report [55]. The aggregates were inserted within droplets containing thiol, DTX, and BSA at an orifice (0.3 MPa). These droplets were then injected into a heated photoionization flow reactor (185-nm UV lamp installed inside while covered with electrically heated quartz mantle). In the reactor, photoionization of the outermost Cu particles enabled CuSH– formation due to electrostatic interaction between the positively charged (*i.e.*, photoionized) Cu particles and negatively charged thiol groups and subsequent thermal solvent extraction from the droplets derived co-aggregation of the thiolated aggregates and adjacent DTX-BSA components in a single-pass gas flow, resulting in the formation of nanoscale multi-component supraparticles.

The part of the particle-laden flow was sampled directly to obtain the aerosol size distributions using an SMPS (3936, TSI, USA), and the data

were recorded using Aerosol Instrument Manager® software. The resulting particles were collected on a polytetrafluoroethylene membrane filter and dispersed in phosphate-buffered saline (PBS) to measure direct light scattering (DLS; Nano-S90 ZetaSizer, Malvern Instruments, UK) as well as the light absorption and increase in photothermal temperature using a UV-vis spectrophotometer (U-2800, Shimadzu, Japan) and photothermal imaging camera (Therm-App, Israel) with an 808-nm NIR laser (Changchun New Industries, China), respectively. The photothermal conversion efficiency of FeZnCuS@DTX-BSA was estimated using the formula in previous reports [56–58]. The shape and microstructure of the resulting particles were observed by TEM (Tecnai G2 F20 S-TWIN, FEI, USA) after placing the resulting particles on carbon-coated copper grids (Ted Pella, Inc., USA) using a mini particle sampler (Ecomesure, France). The surface state of the individual inorganic particles was analyzed by XPS (K-Alpha, Thermo Scientific, USA). The crystallinity of Fe, Zn, and CuS and BSA incorporation were also identified using X-ray diffractometry (DIATOME, PANalytical, UK) and Raman spectroscopy (XPLORA™, Horiba, Japan), respectively. The composition of the resulting particles was identified using an SEM-EDX (S-4800, Hitachi, Japan) while surface functional groups were analyzed by FTIR (Nicolet iS10, Thermo Scientific, USA) spectroscopy.

## 2.2. LC and *in vitro* DOX release

DTX was loaded in the resulting particles. The separation of DTX from the particles was analyzed using a centrifugal ultrafiltration device (Amicon, Millipore, USA) and a UV-vis spectrophotometer. The DTX released from the resulting particles at pH 6.5 (acetate buffered saline (ABS), simulating tumor microenvironment) and 7.4 (PBS, simulating physiological condition) was monitored for 24 h in the absence and presence of NIR irradiation. The particles were inserted into a dialysis bag ( $MWCO = 3.5$  kD; Spectrum Laboratories, USA) and immersed in a tube containing 25 mL of ABS and PBS. High-performance liquid chromatography (1260 Infinity II, Agilent Technologies, USA) was used to determine the amount of DTX released from the particles at pre-determined time intervals using a C18 reversed-phase column (GL Sciences, Japan).

## 2.3. Cellular uptake

The EMT6 cell lines were cultured in Dulbecco's high-glucose modified Eagle's medium (GE Healthcare Life Sciences, USA) supplemented with fetal bovine serum (10 %), penicillin G sodium, and streptomycin sulfate (1 %) in a humidified incubator (37 °C, 5 % CO<sub>2</sub>). EMT6 cells ( $2 \times 10^5$  cells) were cultured on each well of 12-well plates and kept overnight for adhesion. After 24 h, the cells were exposed to

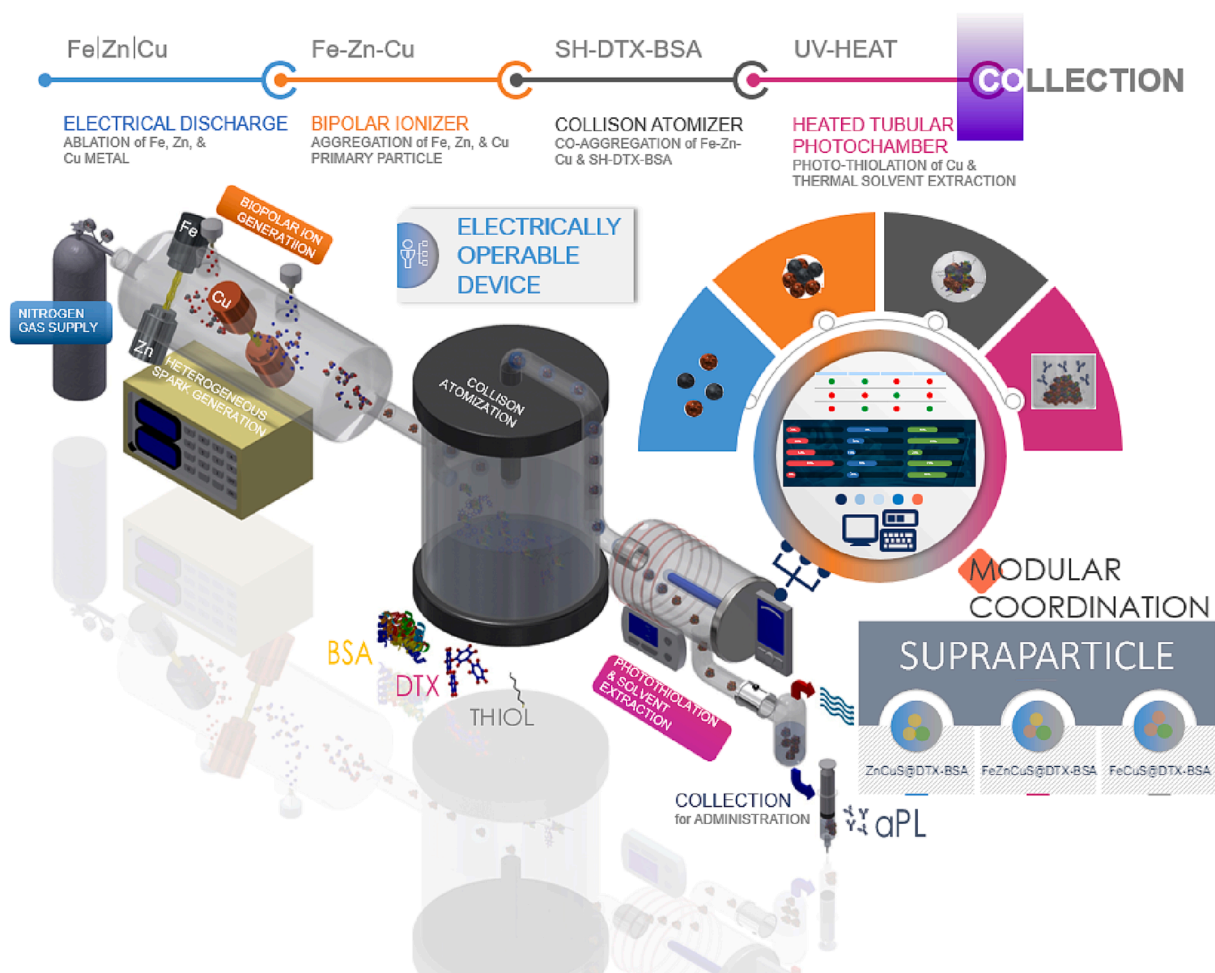


**Fig. 1.** Illustration of the AAM for the spontaneous plug-in assembly of the multi-component supraparticles. Fe (Zn or Fe–Zn)–Cu aggregates formed by ablation-condensation from atmospheric electrical discharges in the presence of bipolar gaseous ions were inserted within droplets containing 1-hexanethiol, DTX, and BSA in a nitrogen gas flow. The aggregate-inserted droplets were then passed through a heated photoionization flow reactor to derive CuSH– formation and their co-aggregation with DTX-BSA during thermal solvent extraction in the gas flow to form multi-component supraparticles. The resulting supraparticles were incorporated further with aPL to secure the chemo-chemodynamic-photothermal-immuno antitumor effects.

coumarin-6 (1  $\mu\text{g/mL}$ )-loaded supraparticles (3  $\mu\text{g/mL}$ ) and incubated for 90 min. The cells were washed, trypsinized, and suspended in PBS after 2 h for flow cytometry (FACSCalibur, BD Biosciences, USA).

#### 2.4. ROS generation

EMT6 cells ( $2 \times 10^5$ ) were cultured in each well on 12-well plates, incubated overnight for adhesion, and exposed to the supraparticles for 24 h. NIR exposure (1  $\text{W/cm}^2$ , 3 min) was conducted for the relevant treatment groups after 2 h of particle exposure. The cells were treated with 2',7'-dichlorodihydrofluorescein diacetate (DCFDA) for 1 h and washed twice with PBS, trypsinized, and resuspended in the buffer for flow cytometry. The levels of ROS in the cells were compared by computing the green fluorescence.

#### 2.5. Apoptosis

EMT6 cells ( $2 \times 10^5$ ) were cultured in each well on 12-well plates, left to adhere overnight, and incubated with the supraparticles for 48 h. NIR irradiation (1  $\text{W/cm}^2$ , 3 min) was performed for the relevant treatment groups after 2 h of exposure. The cells were washed twice with PBS, trypsinized, resuspended in binding buffer with propidium iodide (PI) and Annexin V-fluorescein isothiocyanate (FITC), incubated for 15 min in the dark, and resuspended in the buffer for flow cytometry.

#### 2.6. Cytotoxicity

EMT6 cells ( $1 \times 10^4$ ) were seeded in each well of 96-well plates and incubated for 24 h. The cells were exposed to the supraparticles for 24 h, including free DTX for comparison. The relevant treatment groups were irradiated with NIR (1  $\text{W/cm}^2$ , 3 min) after 2 h of the supraparticle exposure. The treated cells were washed with PBS and treated further with 50  $\mu\text{L}$  of an MTT (Sigma-Aldrich, USA) solution (2.5  $\text{mg/mL}$ ) for 6 h. Dimethyl sulfoxide (100  $\mu\text{L}$ ) was injected into the formed formazan crystals to obtain the absorbance at 570 nm using a microplate reader (Thermo Scientific, USA).

#### 2.7. Biodistribution and in vivo photothermal activity

Cy5.5 tagged supraparticles, including free Cy5.5 (1  $\mu\text{g/mL}$ ) for comparison, were administered intravenously into subcutaneous EMT6 tumor-bearing BALB/c mice for *in vivo* and *ex vivo* imaging of the principal organs (heart, lung, liver, kidney, and spleen) and tumors through Fluorescence-labeled Organism Bio-imaging Instrument (FOBI, Neoscience, South Korea). After 24 h, the mice were sacrificed. The organs and tumors were harvested for *ex vivo* imaging. nEO iMAGING software was used for fluorescence intensity analysis after positioning the organs and tumors in the imaging system.

#### 2.8. Histopathology

The tumors and principal organs were harvested from the sacrificed mice after the study period (21 days). They were sliced (3–4  $\mu\text{m}$ ), embedded in paraffin, and stained with hematoxylin and eosin (H&E) for optical microscopy (Eclipse 80i, Nikon, Japan).

#### 2.9. In vivo antitumor study

A subcutaneous inoculation of EMT6 cells ( $1 \times 10^6$ ) was conducted in 5–6 week-old female BALB/c nude mice to develop the EMT6 xenograft model. The mice were divided into six groups ( $n = 6$ ) after the volume reached  $\sim 100 \text{ mm}^3$  in 10 days. The mice were administered an intravenous injection of FeZnCuS@DTX-BSA with and without aPL (1.5  $\text{mg/kg}$ ). For comparison, free aPL and DTX (2  $\text{mg/kg}$ ) were administered at an equivalent dose every-three days (10th, 13th, and 16th day). NIR laser was applied to the tumor after 24 h of administration for the

relevant treatment groups. The body weight and tumor volumes were measured every-three days while the tumor volume was calculated through the formula ( $1/2 \times \text{longest dimension} \times \text{shortest dimension}^2$ ). The dimensions were obtained using Vernier calipers.

The hemolytic profiles of FeZnCuS@BSA and FeZnCuS@DTX-BSA were acquired with different concentrations (100–1000  $\mu\text{g/mL}$ ) for 8 h at 37  $^\circ\text{C}$ . For blood chemistry, Institute of Cancer Research mice randomly divided into two groups ( $n = 5$ ): saline and FeZnCuS@DTX-BSA configurations. Except for the control, the mice were intravenously injected with 150  $\mu\text{L}$  of saline with a dose of an equivalent amount of 10  $\text{mg}$  of DTX per kilogram of the mouse (five times more than the dose that used in the *in vivo* antitumor study). After 15 days, the mice were sacrificed, and the blood samples were compiled for a complete blood panel and blood biochemistry analyses.

#### 2.10. Immunohistochemistry

After the antitumor study period, the tumors were excised and trimmed in slices to examine the expression of the apoptotic markers (C-Caspase-3 and C-PARP), tumor cell proliferation marker (Ki-67), and angiogenesis marker (CD31). Avidin-biotin-peroxidase complex-peroxidase substrate kit (Vector Labs, USA) was used to determine the fluctuations in the immunoreactivity from the tumor masses through purified primary antibodies against HMGB1 (ICD marker), CRT (ICD marker), CD4 (effector T cell infiltration marker), and CD8 (effector T cell infiltration marker). A positive result was defined as  $>20\%$  of the tissues were stained with immunoreactivity marker. HMGB1- and CRT-positive cells ( $\%/\text{mm}^2$  of tumor mass) as the percentage of coverage in the tumor masses, along with tumor-infiltrated CD4 and CD8 immunostained cells ( $\text{cells}/\text{mm}^2$  of tumor mass) were assessed by an automated image analyzer.

All mice experiments were approved and followed the instructions and guidelines of the Institutional Animal Ethics Committee, Yeungnam University, Republic of Korea. The measurements were performed with the mean  $\pm$  SD. The statistical significance between the groups was evaluated using a Student's *t*-test and one-way analysis of the variance; *p* values  $< 0.05$  were considered significant.

### 3. Results and discussion

The co-aggregation was first determined by measuring the in-flight size distributions before and after incorporating metallic aggregates and mixture droplets, including after passing over the heated photoionization flow reactor. The distribution results were obtained by sampling the part of particle-laden flow using a scanning mobility particle sizer (SMPS), as shown in Fig. S2A. The metallic aggregates (FeCu, ZnCu, or FeZnCu) as backbone particles exhibited comparable size distributions representing no significant differences in geometric mean diameter (GMD), geometric standard deviations (GSD), and total number concentration (TNC). On the other hand, the mixture droplet had larger GMD and GSD values than the backbone particles, suggesting the backbone particles can be inserted into the droplets at a nozzle of the atomizer. After passing over the photoionization reactor, TNCs of the incorporated configurations were reduced significantly by approximately  $7.7 \times 10^6 \text{ particles}/\text{cm}^3$ . Nevertheless, no significant differences in the distribution between the configurations (FeCuS@DTX-BSA, ZnCuS@DTX-BSA, and FeZnCuS@DTX-BSA) were observed even with no satellite peaks, as shown in the right-side panel of Fig. S2A, suggesting that the developed AAM is workable for co-aggregation of the backbone particles and components in the mixture droplets without distribution distortion after the photoreaction, even in the single-pass flow.

The morphologies of the three co-aggregated configurations were observed by transmission electron microscopy (TEM) after collecting the resulting particles on carbon-coated copper grids and placing them in a mini particle sampler. As shown in Fig. 2A, the dotted spherical particles



(approximately 120 nm in lateral dimension) were distributed in broad outline, where several-nanometer-sized particles were densely dotted on the spherical domains, similar to the supraparticles in a previous report [26], as shown in the middle-magnification images. Differences in the arrangement of the dot particles in the domains may be because of a structural difference of the backbone particles also examined by TEM (Fig. S2B; dendritic for ZnCu, dotted for FeCu, and a cross between the dendritic and dotted for FeZnCu), which were attributed to the formation of different core textures, resulting in the different co-aggregation behaviors in the heated photoionization flow reactor. Nevertheless, the insertion of the backbone particles into the mixture droplets at the atomizer nozzle ensured the formation of supraparticles for the different backbone particles as a modulatable process, even without considering the different reduction potentials of constituent metallic components. The characteristic lattice fringes of Fe ( $d_{\text{Fe}, 110} = 0.203$  nm), Zn ( $d_{\text{Zn}, 101} = 0.242$  nm), and CuS ( $d_{\text{CuS}, 100} = 0.320$  nm) were identified in the high-magnification images for the outermost region of the supraparticles, and no FeS and ZnS were detected. This may be due to the surface-confined approach of the photons from the photoionization reactor at room temperature under flowing nitrogen gas for sulfidation of the outermost Cu particles (positively charged (i.e., electron detached) from photon attacks) and to the strong affinity between the photoionized Cu and negatively charged -SH. The zero-valent surface states of Fe (2p) and Zn (2p) in core-level X-ray photoelectron spectroscopy (XPS) supported the surface-confined sulfidation (Fig. S3A). The only oxidized states of the outermost Cu (2p) adsorbed the negatively charged -SH of R-O-SH groups [59], which induced a shouldering of the major S 2p band representing the existence of sulfide and a satellite band at around 168 eV [60]. The XRD profile of FeZnCuS@DTX-BSA exhibited the characteristic bands for the individual Fe, Zn, and CuS (Fig. S3B) [61–63], supporting that the supraparticles consisted of crystalline Fe, Zn, and CuS particles. The characteristic bands at around 1000, 1450, and 1650  $\text{cm}^{-1}$  in the Raman spectrum (Fig. S3B) matched the functional groups of BSA observed in a previous study [64], proving the passivation of FeZnCuS by BSA. The dotted spherical characteristics and outermost Cu sulfidation were observed by scanning electron microscopy (SEM) and energy-dispersive X-ray spectroscopy (EDX), respectively (Fig. S3C), where the Cu and S contents for the supraparticles were consistently 36 % and 8 %, respectively, despite the change in backbone particle composition, further supporting the modular property of the developed AAM.

The modular property of the AAM was evaluated by constructing FeZnCuS@DTX-BSA with increased backbone particle size and DTX-BSA content to secure a different core texture and overlayer structure. Fig. S4A shows low- and high-magnification TEM images of FeZnCuS aggregates assembled under a five times slower nitrogen gas flow rate, which consisted of Fe(110), Zn(101), and CuS(100) particles, as are the components in existing supraparticles. Suprastructuring of the approximately 10 nm constituent particles and subsequent co-aggregation with DTX-BSA in the heated photoionization flow reactor constructed another type of supraparticles (Fig. S4B). Fig. S4C shows supraparticles from an assembly condition with increasing backbone particle size and DTX-BSA content (30 wt%), where the high-magnification image shows a darker particle sufficiently to shade the constituent particles because of a thicker DTX-BSA overlayer deposited on the backbone particle. High-magnification TEM (Fig. S4D) revealed the overlayers for three different contents of DTX-BSA (30–50 wt%), where the constituent metallic particles were completely passivated by DTX-BSA matrices, further supporting the modular property of the AAM to a variety of conditions of the backbone particles and DTX-BSA overlayers for supraparticle assembly.

Light absorption profiles of the supraparticles (FeCuS@DTX-BSA, ZnCuS@DTX-BSA, and FeZnCuS@DTX-BSA) were obtained by UV–Vis spectrophotometry after the collected particles were dispersed in PBS. As shown in Fig. S5A, the absorbance band of the particles was located at 980 nm, which matched the characteristic band of CuS nanoparticles [65], proving sulfidation of the outermost Cu particles. The combination

between the CuS and other metals (Fe, Zn, or Fe–Zn) also induced broad-spectrum light absorption, which may absorb the wavelengths of both NIR I (650–950 nm) and II (1000–1350 nm) to be flexible in photothermal conversion [66,67]. Temperature elevations of the supraparticle dispersions under NIR (808 nm) irradiation with three different power densities (1.0, 1.5, and 2.0  $\text{W}/\text{cm}^2$ ) were recorded for 3 min. The temperatures of the irradiated spots on ZnCuS@DTX-BSA, FeCuS@DTX-BSA, and FeZnCuS@DTX-BSA dispersions reached 45.1, 51.6, and 56.2 °C after 3 min of NIR exposure, respectively, as shown in Fig. 2B and Fig. S5B. In addition, at a fixed power density (1.0  $\text{W}/\text{cm}^2$ ), the highest temperatures (39.1, 44.6, and 50.0 °C for the three dispersions) were maintained, even after five on (3 min)–off (3 min) irradiation cycles (Fig. S5C). Although the temperature elevations were related to the photothermal conversion activity of the CuS component in the supraparticles, FeZnCuS@DTX-BSA exhibited the greatest activity compared to the other configurations. This was probably caused by a better interband transition between the unoccupied and occupied bands of FeZnCuS (trimetallic) than those of the others (bimetallic) that generates broadened working bandwidth for enhancement in photothermal conversion activity [68,69]. The difference in photothermal conversion between ZnCuS@DTX-BSA and FeCuS@DTX-BSA was likely due to the more suitable NIR absorption profile of FeCuS than ZnCuS [70–72]. The photothermal conversion efficiency of FeZnCuS@DTX-BSA upon NIR irradiation was  $52.8 \pm 1.2$  %, which was comparable to Au–Ag alloy nanoparticles used for anticancer therapy in a previous report [56].

To conduct proper comparisons between the supraparticles, the loading capacity of DTX was set to approximately 10 % (Fig. S6A), which was achieved by constructing comparable size and composition (described above) between the supraparticles from modulatable properties of the developed AAM. The DTX loading was also examined by Fourier transform infrared (FTIR) spectroscopy, as shown in Fig. S6B. The FTIR profiles exhibited the representative bands of DTX at around 1720 and 1260  $\text{cm}^{-1}$  attributing to C=O and C–O stretchings, respectively [73,74]. The differences in the characteristic band intensity between the supraparticles at the identical loading capacity (LC) might be because of the differences in core texture between the supraparticles (refer to Fig. 2A) that generate locational differences for DTX deposition on the backbone particles during the co-aggregation. pH- and NIR-responsive release profiles were obtained to examine the release behavior of loaded DTX, as shown in Fig. S6C and S6D. Similar tendencies were observed in the profiles at pH 7.4 (simulating the physiological condition) and pH 6.5 (simulating tumor microenvironment), whereas all supraparticles exhibited cumulative releases lower than half of the total DTX loaded for 48 h. This may be because of the successful co-aggregation of DTX-BSA as complex matrices that inhibit the immediate release of DTX for sustainability. In the case of NIR irradiation, burst releases of DTX were obtained for every cycle (3 min NIR exposure after 1, 4, and 7 h incubation), where most of the loaded DTX (>90 %) were released after 10 h of incubation at tumor microenvironment pH, suggesting that the supraparticles warrant NIR-responsive on-demand release of hydrophobic chemodrugs.

Cellular internalization of the three supraparticles (FeCuS@DTX-BSA, ZnCuS@DTX-BSA, and FeZnCuS@DTX-BSA) was determined by fluorescence-activated cell sorting (FACS). Briefly, 3  $\mu\text{g}/\text{mL}$  of each supraparticle was incubated with EMT 6 cells for 2 h. FACS showed that FeZnCuS@DTX-BSA had the highest mean fluorescence intensity (MFI) (Fig. 3A). The results matched the order of characteristic band intensity of BSA (FeZnCu@DTX-BSA > FeCu@DTX-BSA > ZnCu@DTX-BSA) at approximately 1650 and 2950  $\text{cm}^{-1}$  [75], which might be due to surface dominance of DTX-BSA (Fig. S6B) probably caused by the difference in the core texture (Fig. 2A). The *in vitro* cytotoxicity was examined after 24 h treatment with supraparticles in the absence and presence of NIR irradiation, including free DTX for comparison using a 3-(4,5-dimethylthiazol-2-yl)-2,5-diphenyltetrazolium bromide (MTT) assay. All supraparticles without NIR exhibited a dose-dependent cytotoxicity (Fig. S7A), and slightly greater cytotoxicity was observed than that of

free DTX due to the combinatorial effects of the Fenton/Fenton-like reaction (chemodynamic effect) and DTX release (chemotherapeutic effect). NIR irradiation enhanced the cytotoxicity significantly on EMT 6 cells because the photothermal effect enhanced the rate of the Fenton/Fenton-like reactions. The order of cytotoxicity of the three supraparticles was  $\text{FeZnCuS@DTX-BSA} > \text{FeCuS@DTX-BSA} > \text{ZnCuS@DTX-BSA}$ , which was consistent with the order of photothermal conversion and cellular internalization, representing a stable performance of the resulting supraparticles from the developed AAM. In connection with the cytotoxicity, ROS generation after incubation of the cells treated with the supraparticles was confirmed, where the generation level also followed the order for cytotoxicity, even with NIR irradiation (Fig. 3B). The ROS generation from Fe-included configurations were greater than the counterpart (i.e.,  $\text{ZnCuS@DTX-BSA}$ ), supporting the better CDT efficacies of the Fe-included configurations can be derived in the identical dose of DTX because of higher levels of ROS from Fenton reaction [76]. The photothermal effects from NIR irradiation further increased the levels of ROS generation that matched the profiles of cytotoxicity and photothermal temperature elevation. This NIR-reinforced trend was also identified in the apoptosis assay even for 48 h, where the induction of apoptosis was confirmed by flow cytometry to evaluate the live cells, early and late apoptotic cells, and necrotic cells. Differences in apoptosis were observed between the absence and presence of NIR (Fig. S7B); thus, the apoptosis percentage of the treated cells was boosted to approximately 63 % (from 47 % without NIR), 53 % (from 42 %), and 75 % (from 53 %) for  $\text{FeCuS@DTX-BSA}$ ,  $\text{ZnCuS@DTX-BSA}$ , and  $\text{FeZnCuS@DTX-BSA}$  treatments, respectively, in the presence of NIR irradiation (Fig. 3C), showing that the accelerated ROS generation ensued higher apoptosis of cells.

To conduct *in vivo* and *ex vivo* imaging for biodistribution analysis, cyanine (Cy5.5)-labeled supraparticles ( $\text{Cy5.5@FeCuS@DTX-BSA}$ ,  $\text{Cy5.5@ZnCuS@DTX-BSA}$ , and  $\text{Cy5.5@FeZnCuS@DTX-BSA}$ ), including free Cy5.5 were intravenously administered in subcutaneous EMT6

tumor-bearing mice. As shown in Fig. 4A, time-dependent imaging was performed at 0.5, 6.0, 12.0, and 24.0 h postinjection. The Cy5.5-labeled supraparticles were distributed throughout the body (with significant fluorescence in the liver region for the supraparticles and kidney region for the free Cy5.5) until 6.0 h postinjection. With time, the distribution of the supraparticles changed compared to free Cy5.5 probably because BSA enables prolonged circulation time of the supraparticles assisting the enhanced permeability and retention (EPR) effect without the opsonization. This was clarified by *ex vivo* imaging (Fig. 4B) performed with the harvested organs after the initiation of fluorescence decline in the administered mice after 24 h. The resulting images showed that most organs, excluding the kidneys from the supraparticle-treated mice, have a greater fluorescence than those of free Cy5.5 treated mice due to BSA incorporation. This effect eventually induced a greater tumor accumulation of the supraparticles compared to free Cy5.5, but there were slight differences ( $\text{FeZnCuS@DTX-BSA}$  was the highest according to the highest internalization (Fig. 3A)) in the accumulation between the supraparticles. NIR irradiation ( $1 \text{ W/cm}^2$  for 3 min) was conducted on tumor regions 24 h postinjection, and temperature elevation was monitored during the irradiation (Fig. 4C). The elevation profiles reflected the *in vitro* results for NIR irradiation onto the supraparticle dispersions (Fig. 2B and Fig. S5B), but there were differences in the highest temperature owing to the *in vivo* tumor accumulation. Based on the results collected,  $\text{FeZnCuS@DTX-BSA}$  was the most effective configuration for further *in vivo* antitumor and biosafety studies with the additional incorporation of aPL to potentiate the immune reactions for a durable production of a pool of T cells along with ICD induced by the Fenton/Fenton-like reaction, DTX release, and photothermal effect.

The most significant tumor ablation was expected after the administration of  $\text{FeZnCuS@DTX-BSA}$  with NIR and aPL, as shown in Fig. S8A, even though DTX also has tumor inhibition capability from the chemotherapeutic effect, ICD, and immunogenic modulation [77,78]. The boosted tumor inhibition in the presence of NIR irradiation may be

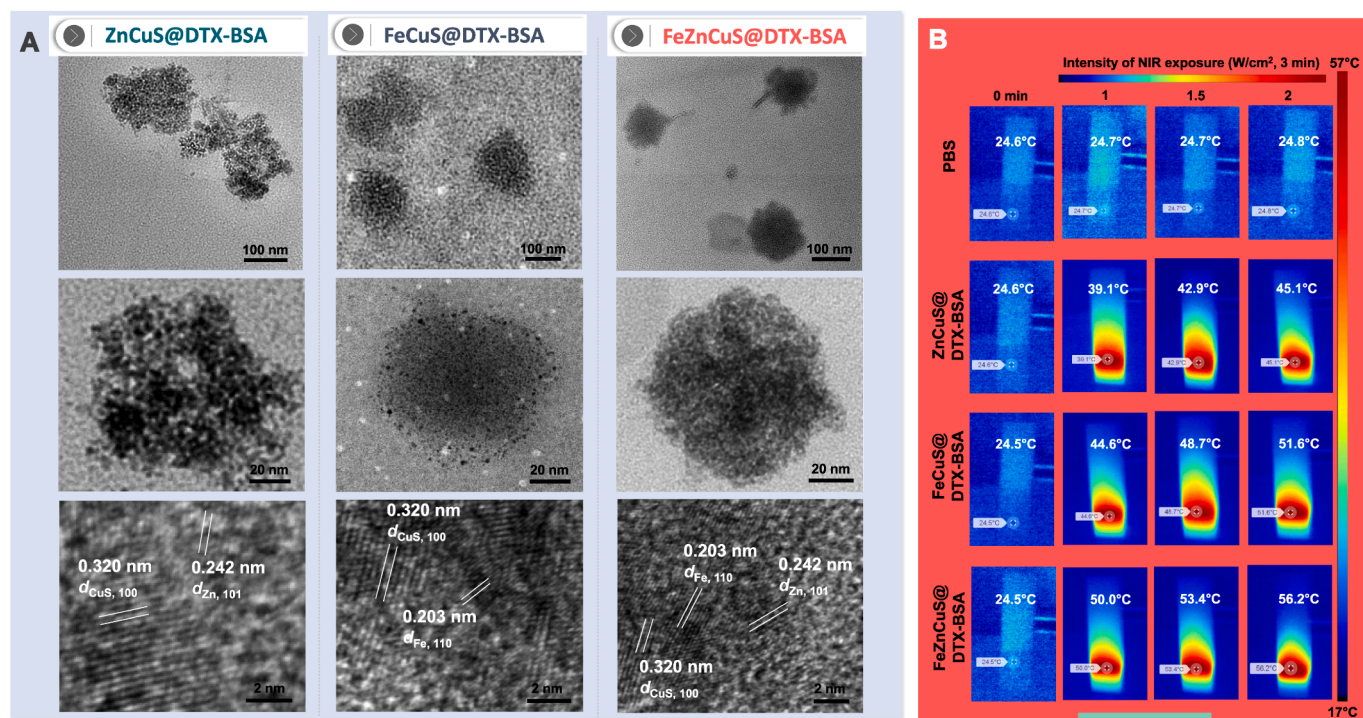


**Fig. 2.** Morphological and photothermal analyses of the resulting supraparticles, including PBS alone for comparison. (A) Low- and high-magnification TEM images of  $\text{FeCuS@DTX-BSA}$ ,  $\text{ZnCuS@DTX-BSA}$ , and  $\text{FeZnCuS@DTX-BSA}$ . The lattice spacings in the high-magnification images of the supraparticles matched the individual Fe (Zn or Fe and Zn) and CuS particles. Modulating the electrical discharge operations from Zn–Cu to Fe–Zn–Cu configurations induced a difference in the shape of the supraparticles and the distribution of the individual particles. (B) Photothermal images were recorded upon NIR irradiation for 3 min with different irradiation intensities ( $1\text{--}2 \text{ W/cm}^2$ ) onto the three supraparticle dispersions.

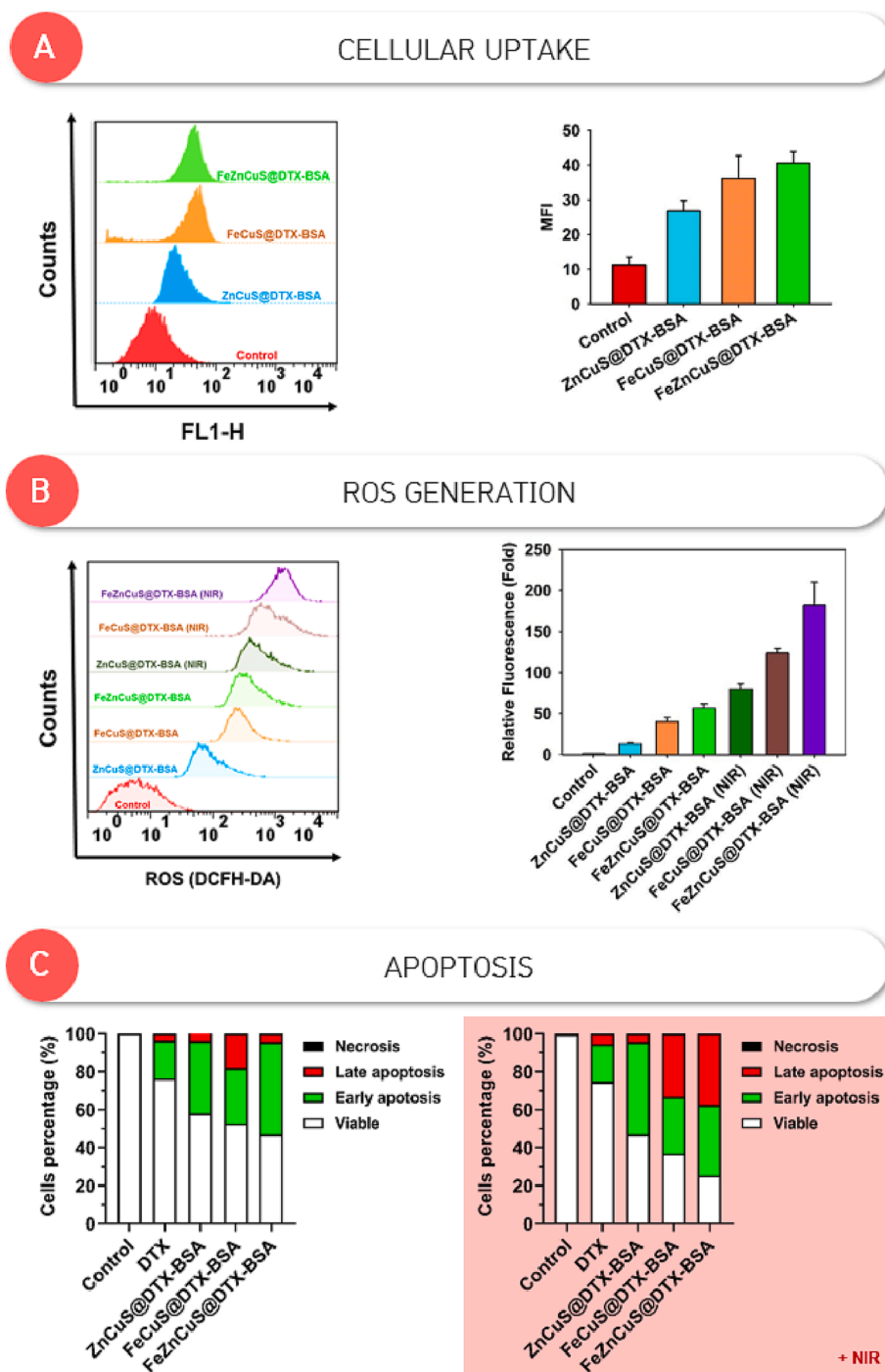


**Fig. 3.** Cellular uptake, ROS generation, and apoptosis of the resulting supraparticles. (A) FACS profiles and their quantified plots to represent cellular internalization of the supraparticles. Uptake of DTX alone (5  $\mu\text{g/mL}$ ) for 60 min was selected as the control for comparison, while coumarin-6 was used for staining. (B) DCFDA profiles and quantified plots to represent ROS generation. (C) Fractional bar plots illustrating the apoptotic status of the EMT6 cells treated with the supraparticles for 24 h in the absence and presence of NIR irradiation (1 W/cm<sup>2</sup>, 3 min). An equivalent DTX (1  $\mu\text{g/mL}$ ) was selected for comparison.

accredited to the individual (Fenton/Fenton-like reaction, photothermal effect, DTX release, and immunogenic modulation) and combinatorial (photothermal acceleration of the Fenton/Fenton-like reaction and photothermal and chemodrug induced ICD) therapeutic effects [79]. Despite the combinatorial effects, even with NIR irradiation, there were similar body weight profiles in every treatment group, showing no abnormal alterations (Fig. S8B) with a 100 % survival rate throughout the study period (Fig. S8C). Histopathological imaging (Fig. S8D) of the major organs treated with I–VI configurations also did not show any abnormal signs of toxicity or serious side effects, even though the necrotic signs in the tumor after the treatments were increasing according to the order of the tumor inhibition, proving biosafety of the supraparticles and their operation strategies.

The tumor cell volume (TCV) with apoptotic, cell proliferation, and angiogenesis markers were analyzed (Fig. 5A) and quantified (Fig. 5B). Expression of the TCV reduction and apoptotic markers (C-caspase-3 and C-polyadenosine diphosphate-ribose polymerase (PARP)) was intensified in the order of I < II < III < IV < V < VI. In contrast, the expression order of cell proliferation (Ki-67) and angiogenesis (CD31) markers was inversely as expected. The ICD markers and effector T cells tumor filtration were further imaged and quantified through immunohistochemical staining (Fig. 6A and 6B). HMGB1 and CRT expression trends followed apoptotic markers, where the signs from free DTX treatment (II) enhanced by embedding in supraparticles were strengthened by the chemo-chemodynamic effect (III). The intratumoral ICD markers were escalated further in the presence of NIR from the photothermal-induced



ICD (IV). The higher expression of ICD markers is ineffective if the effector T cells infiltration to the tumors is not enhanced. Therefore, CD4 and CD8 immunolabeled tumoral cells were also examined. Immunogenic modulation with slightly higher numbers of CD4 and CD8 (effector T) cells was achieved after the DTX treatment, which improved marginally after the FeZnCuS@DTX-BSA treatment. Immunomodulation was achieved in the treatment groups; however, the degree of immunomodulation was considerably higher in the cases of NIR and aPL incorporation by complementing each other for better antitumor immune efficacy (Fig. 6C).

The disintegration of FeZnCuS@DTX-BSA supraparticles during five cycles of NIR irradiation (3 min) was observed by TEM to examine the

possibility of renal excretion of constituent metallic particles after use in anticancer treatment (Fig. 7). The low- and high-magnification images revealed the deformation of embedded metallic particles (dark dots on the spherical domains) upon NIR irradiations because of photothermal shrinkage of the DTX-BSA matrices, where the constituent particles (<5 nm; appropriate for renal excretion) were distributed individually after the fifth irradiation cycle. In particular, the temperature increases upon NIR irradiation led to thermal softening of the co-aggregated DTX-matrices (from the local temperatures around constituent particles higher than the critical solution temperature of BSA) [80,81] that facilitate a decrease of the stiffness of the molecular chains to be collapsed. This suggests that NIR irradiation can enhance the rate of the

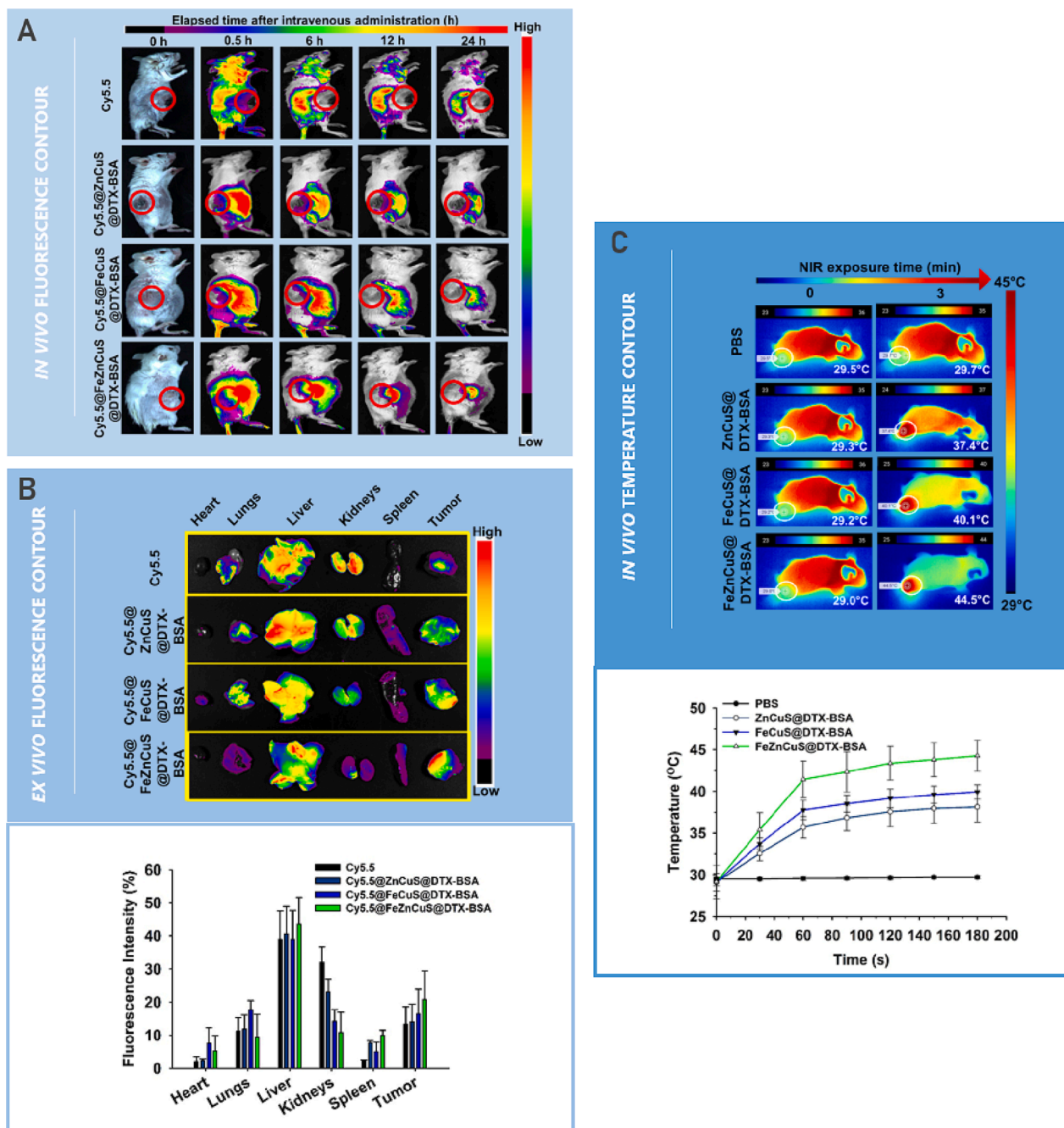


**Fig. 4.** In vivo and ex vivo biodistributions, including photothermal temperature elevation of EMT6 tumor xenografted BALB/c mice after administration. (A) In vivo Cy5.5 fluorescence (100  $\mu$ L) contour images after loading on the supraparticles. The distribution of free Cy5.5 (1  $\mu$ g/mL) was assessed for comparison. (B) Fluorescence images (upper) and their quantified plots (lower) of excised major organs and tumors from the treated mice after 24 h postinjection. (C) Time-dependent photothermal contours and their plots of the mice irradiated NIR (1 W/cm<sup>2</sup>) for 3 min 24 h after injecting the supraparticles.



Fenton/Fenton-like reaction for antitumor therapy and accelerate the collapse of suprastructure for efficient clearance from the body. In addition, the stability of the supraparticle suspension was examined using DLS for 48 h in different media (water, PBS, Roswell Park Memorial Institute (RPMI), and fetal bovine serum (FBS)) by monitoring particle size, polydispersity index (PDI), and zeta potential (Fig. S9). The data exhibited no significant alterations after the dispersal during measurements, suggesting that AAM of the supraparticles and subsequent dispersing in liquid media before their administration may be a viable option for this type of applications. In the case of hemolysis, the resulting supraparticles did not induce significance (<5%), even at the highest dose (Fig. S10). The blood chemistry results exhibited that FeZnCuS@DTX-BSA treated group (10 mg/kg DTX) did not induce significant alterations in blood parameter compared to saline-treated group

(control) after 15 days of systemic administration (Fig. S11). These outcomes coincided with the profiles of body weight (Fig. S8B), survival (Fig. S8C), and histopathological analysis of vital organs (Fig. S8D). Therefore, it is a viable option to minimize the issues of clinical translation and toxicity in the body.

#### 4. Conclusion

An AAM for the continuous plug-in assembly of the multi-component supraparticles was developed and used to derive chemo–chemodynamic–photothermal–immuno cancer therapy. The supraparticles were assembled spontaneously through co-aggregation of Fe (Zn or Fe–Zn)–Cu aggregates and thiol-DTX-BSA mixture droplets from a serial connection of electrically operable devices under a single-pass gas

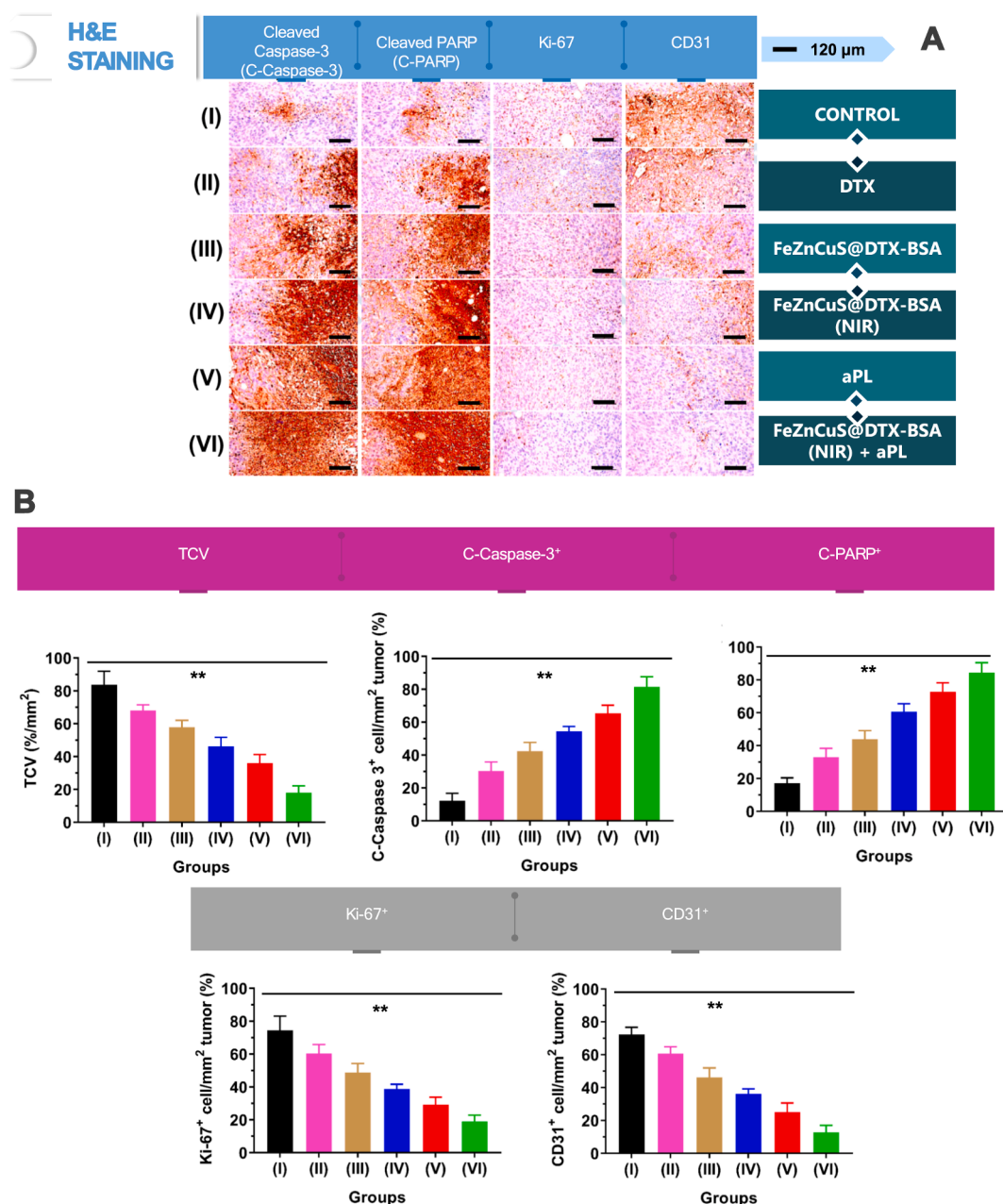


**Fig. 5.** Immunohistochemical examination and quantitative plots of the relevant indicators after the different treatments 24 h postinjection (I: control; II: DTX; III: FeZnCuS@DTX-BSA; IV: FeZnCuS@DTX-BSA (NIR); V: aPL; and VI: FeZnCuS@DTX-BSA (NIR) + aPL) in the absence and presence of NIR irradiation (1 W/cm<sup>2</sup>, 3 min). (A) Optical microscope images were acquired after H&E staining of tumor cell volumes treated with different configurations. Scale bars, 120  $\mu$ m. (B) Percentage plots of TCV, C-Caspase-3, C-PARP, Ki-67, and CD31 in the treated tumor masses. The results are expressed as mean  $\pm$  SD. \*\*  $p < 0.01$ .

flow because of fine particles in the aerosol state exhibit a significantly stronger diffusion behavior for aggregation than those in an aqueous state. The electrostatic collision of Fe (Zn or Fe–Zn) and Cu constituent particles from ablation-condensation could build Fe (Zn or Fe–Zn)–Cu aggregates as backbones of the supraparticles. After the aggregates were inserted within the mixture droplets, the outermost Cu particles (work function = 4.6 eV) were exposed to photons (6.2 eV) from UV-185 nm irradiation to be ionized for electrostatic combination with negatively charged thiol groups and subsequently co-aggregated with the components (DTX for chemotherapeutic and BSA for EPR effects) in the droplets during thermal solvent extraction. The resulting supraparticles

were transferred to *in vitro* (EMT6 cells) and *in vivo* (EMT6 tumor-bearing BALB/c mice) models to determine the workability of the supraparticles, which can be applied for the combination cancer therapy even with aPL for reinforcing efficacy while retaining biosafety. The highest tumor inhibition was achieved using FeZnCuS@DTX-BSA supraparticles, probably due to their highest photothermal effect from the reinforced interband transitions upon NIR irradiation that boosts the ICD and tumor ablation. Immunogenic modulation after aPL addition to FeZnCuS@DTX-BSA was represented by the highest expression of ICD markers and escalated tumoral infiltration of effector T cells, suggesting synergistic enhancement of the tumor inhibition by further adding aPL.

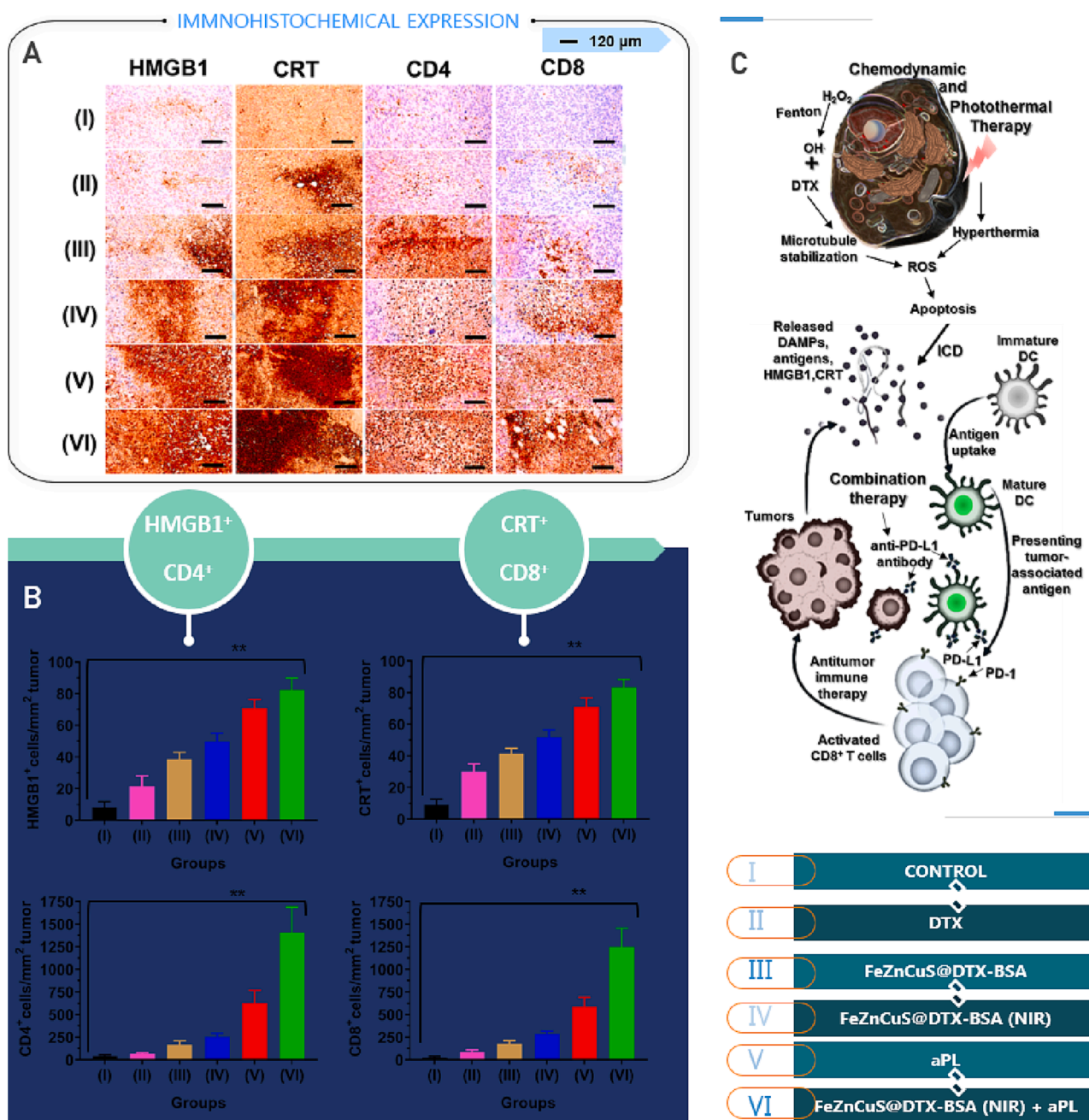


**Fig. 6.** Immunohistochemical expression and quantitative plots of the relevant indicators in the treated tumor masses harvested after 21 days (I: control; II: DTX; III: FeZnCuS@DTX-BSA; IV: FeZnCuS@DTX-BSA (NIR); V: aPL; and VI: FeZnCuS@DTX-BSA (NIR) + aPL) in the absence and presence of NIR irradiation (1 W/cm<sup>2</sup>, 3 min, exposed to the tumor region 24 h postinjection), including a plausible treatment mechanism. (A, B) Immunohistochemical images and HMGB1, CD4, CRT, and CD8 levels in the tumor masses. Scale bars, 120  $\mu$ m. The results are expressed as mean  $\pm$  SD. \*\*p < 0.01. (C) A plausible mechanism for chemo-chemodynamic-photothermal-immuno anticancer therapy upon administration of FeZnCuS@DTX-BSA with aPL. The apoptotic cells released HMGB1 and CRT that may derive immunotherapeutic action through dendritic cell (DC) maturation and CD8<sup>+</sup> T cell activation after adding aPL to the supraparticles.

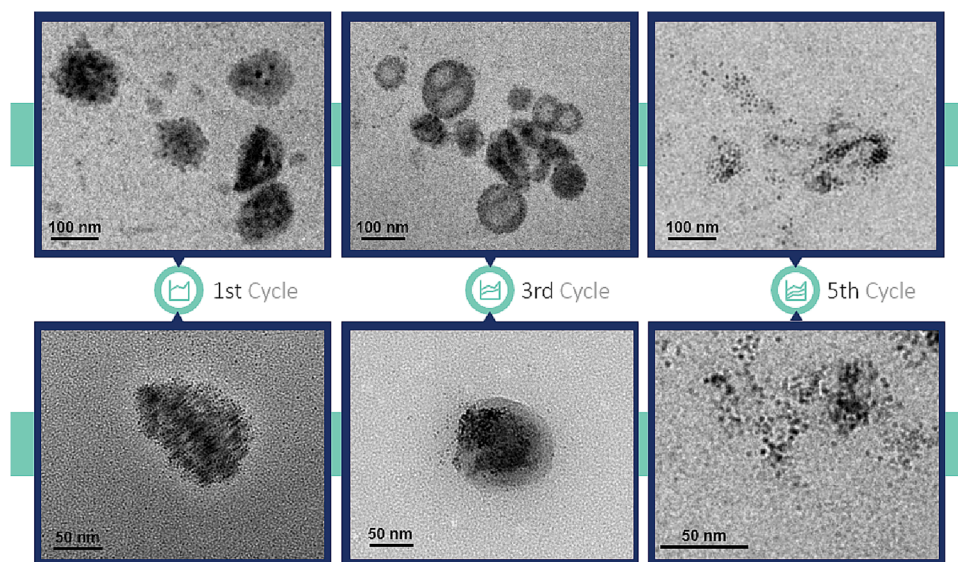


**Fig. 7.** Low- and high-magnification TEM images of disintegrated FeZnCuS@DTX-BSA supraparticles from a repetitive NIR irradiation ( $1 \text{ W}/\text{cm}^2$ , 3 min, five cycles) at acidic pH (6.5).

The results showed that the spontaneously assembled supraparticles from an AAM could provide chemo–chemodynamic–photothermal–immuno cancer therapy in a modular and digitizable configuration to be connected with artificial intelligence platforms for smart cancer nanotherapeutics.

#### CRediT authorship contribution statement

**Sungjae Park:** Methodology, Validation, Formal analysis, Investigation, Data curation, Writing – original draft. **Kishwor Poudel:** Methodology, Validation, Formal analysis, Investigation, Writing – original draft. **Jiseok Lim:** Methodology, Validation, Funding acquisition, Investigation, Writing – original draft. **Jaeho Oh:** Validation, Investigation, Visualization. **Sae Kwang Ku:** Validation, Investigation, Visualization. **Jungho Hwang:** Methodology, Validation, Funding acquisition, Writing – review & editing, Supervision. **Jong Oh Kim:** Investigation, Validation, Supervision, Funding acquisition, Writing – review & editing. **Jeong Hoon Byeon:** Methodology, Validation, Data curation, Conceptualization, Writing – review & editing, Project administration, Supervision.

#### Declaration of Competing Interest

The authors declare that they have no known competing financial interests or personal relationships that could have appeared to influence the work reported in this paper.

#### Data availability

Data will be made available on request.

#### Acknowledgements

This research was supported by the National Research Foundation of Korea (NRF) funded by the Ministry of Science, ICT and future Planning (No. 2022R1A2C1009389, No. 2021R1A6A1A03039493, and No. 2021R1A2C3009556). This work was also supported by Korea Environment Industry & Technology Institute (KEITI) through Technology Development Project for Biological Hazards Management in Indoor Air Program (2021003370005) and Core Technology Development Project for Environmental Diseases Prevention and Management Program (ARQ202201527001), funded by Korea Ministry of Environment

(MOE).

#### Appendix A. Supplementary data

Supplementary data to this article can be found online at <https://doi.org/10.1016/j.cej.2023.142971>.

#### References

- [1] N. Boehnke, J.P. Straehla, H.C. Safford, M. Kocak, M.G. Rees, M. Ronan, D. Rosenberg, C.H. Adelman, R.R. Chivukula, N. Nabar, A.G. Berger, N.G. Lamson, J. H. Cheah, H. Li, J.A. Roth, A.N. Koehler, P.T. Hammond, Massively parallel pooled screening reveals genomic determinants of nanoparticle delivery, *Science* 377 (2022) eabm5551.
- [2] J. Xu, R. Shi, G. Chen, S. Dong, P. Yang, Z. Zhang, N. Niu, S. Gai, F. He, Y. Fu, J. Lin, All-in-one theranostic nanomedicine with ultrabright second near-infrared emission for tumor-modulated bioimaging and chemodynamic/photodynamic therapy, *ACS Nano* 14 (2020) 9613–9625, <https://doi.org/10.1021/acsnano.0c00082>.
- [3] L.u. Zhang, C.-X. Li, S.-S. Wan, X.-Z. Zhang, Nanocatalyst-mediated chemodynamic tumor therapy, *Adv. Healthc. Mater.* 11 (2) (2022) 2101971.
- [4] C. Jia, Y. Guo, F.-G. Wu, Chemodynamic therapy via Fenton and Fenton-like nanomaterials: Strategies and recent advances, *Small* 18 (2022) 2103868, <https://doi.org/10.1002/sml.202103868>.
- [5] N. Wang, C. Liu, W. Yao, H. Zhou, S. Yu, H. Chen, W. Qiao, A traceable, sequential multistage-targeting nanoparticles combining chemo/chemodynamic therapy for enhancing antitumor efficacy, *Adv. Funct. Mater.* 31 (2021) 2101432, <https://doi.org/10.1002/adfm.202101432>.
- [6] T. Wang, H. Zhang, H. Liu, Q. Yuan, F. Ren, Y. Han, Q. Sun, Z. Li, M. Gao, Boosting  $\text{H}_2\text{O}_2$ -guided chemodynamic therapy of cancer by enhancing reaction kinetics through versatile biomimetic Fenton nanocatalysts and the second near-infrared light irradiation, *Adv. Funct. Mater.* 30 (2020) 1906128, <https://doi.org/10.1002/adfm.201906128>.
- [7] M. Liu, Z. Zhang, F. Okejiri, S. Yang, S. Zhou, S. Dai, Entropy-maximized synthesis of multimetallic nanoparticle catalysts via a ultrasonication-assisted wet chemistry method under ambient conditions, *Adv. Mater. Interfaces* 6 (2019) 1900015, <https://doi.org/10.1002/admi.201900015>.
- [8] Y. Zheng, X. Wang, Y. Kong, Y. Ma, Two-dimensional multimetallic alloy nanocrystals: Recent progress and challenges, *CrystEngComm* 23 (2021) 6454–6469, <https://doi.org/10.1039/D1CE00975C>.
- [9] D. Kumar, G.P. Awasthi, C.H. Park, C.S. Kim, Multifunctional trimetallic colloidal plasmonic nanohybrid: Highly efficient photocatalyst and photothermal agent, *Adv. Mater. Interfaces* 5 (2018) 1800331, <https://doi.org/10.1002/admi.201800331>.
- [10] B. Shan, H. Liu, L. Li, Y. Lu, M. Li, Near-infrared II plasmonic phototheranostics with glutathione depletion for multimodal imaging-guided hypoxia-tolerant chemodynamic-photocatalytic-photothermal cancer therapy triggered by a single laser, *Small* 18 (2022) 2105638, <https://doi.org/10.1002/sml.202105638>.
- [11] Y. Wang, L. An, J. Lin, Q. Tian, S. Yang, A hollow  $\text{Cu}_9\text{S}_8$  theranostic nanoplatfrom based on a combination of increased active sites and photothermal performance in enhanced chemodynamic therapy, *Chem. Eng. J.* 385 (2020), 123925, <https://doi.org/10.1016/j.cej.2019.123925>.



- [12] Y. Yao, Z. Huang, T. Li, H. Wang, Y. Liu, H.S. Stein, Y. Mao, J. Gao, M. Jiao, Q. Dong, J. Dai, P. Xie, H. Xie, S.D. Lacey, I. Takeuchi, J.M. Gregoire, R. Jiang, C. Wang, A.D. Taylor, R. Shahbazian-Yassar, L. Hu, High-throughput, combinatorial synthesis of multimetallic nanoclusters, *Proc. Natl. Acad. Sci. U.S.A.* 117 (2020) 6316–6322, <https://doi.org/10.1073/pnas.1903721111>.
- [13] D. Ho, Digital nanomedicine: A new frontier for drug development, *ACS Nano* 16 (2022) 3435–3437, <https://doi.org/10.1021/acsnano.2c01835>.
- [14] A.A. Volk, R.W. Epps, M. Abolhasani, Accelerated development of colloidal nanomaterials enabled by modular microfluidic reactors: Toward autonomous robotic experimentation, *Adv. Mater.* 33 (2021) 2004495, <https://doi.org/10.1002/adma.202004495>.
- [15] Y.S. Choi, H. Jeong, R.T. Yin, R. Avila, A. Pfenniger, J. Yoo, J.Y. Lee, A. Tzavelis, Y. J. Lee, S.W. Chen, H.S. Knight, S. Kim, H.-Y. Ahn, G. Wickerson, A. Vázquez-Guardado, E. Higbee-Dempsey, B.A. Russo, M.A. Napolitano, T.J. Holleran, L. A. Razzak, A.N. Miniovich, G. Lee, B. Geist, B. Kim, S. Han, J.A. Brennan, K. Aras, S. S. Kwak, J. Kim, E.A. Waters, X. Yang, A. Burrell, K.S. Chun, C. Liu, C. Wu, A. Y. Rwei, A.N. Spann, A. Banks, D. Johnson, Z.J. Zhang, C.R. Haney, S.H. Jin, A. V. Sahakian, Y. Huang, G.D. Trachiotis, B.P. Knight, R.K. Arora, I.R. Efimov, J. A. Rogers, A transient, closed-loop network of wireless, body-integrated devices for autonomous electrotherapy, *Science* 376 (2022) 1006–1012, <https://doi.org/10.1126/science.abm1703>.
- [16] H. Canziani, S. Chiera, T. Schuffenhauer, S.-P. Kopp, F. Metzger, A. Bück, M. Schmidt, N. Vogel, Bottom-up design of composite supraparticles for powder-based additive manufacturing, *Small* 16 (2020) 2002076, <https://doi.org/10.1002/sml.202002076>.
- [17] G.L. Goh, H. Zhang, T.H. Chong, W.Y. Yeong, 3D printing of multilayered and multimaterial electronics: A review, *Adv. Electron. Mater.* 7 (2021) 2100445, <https://doi.org/10.1002/aeml.202100445>.
- [18] Y. Pang, Y. Cao, Y. Chu, M. Liu, K. Snyder, D. MacKenzie, C. Cao, Additive manufacturing of batteries, *Adv. Funct. Mater.* 30 (2020) 1906244, <https://doi.org/10.1002/adfm.201906244>.
- [19] C. Ligon, R. Liska, J. Stampfl, M. Gurr, R. Mülhaupt, Polymers for 3D printing and customized additive manufacturing, *Chem. Rev.* 117 (2017) 10212–10290, <https://doi.org/10.1021/acs.chemrev.7b00074>.
- [20] K. Mondal, M.D. McMurtrey, Present status of the functional advanced micro-, nano-printings – A mini review, *Mater. Today Chem.* 17 (2020), 100328, <https://doi.org/10.1016/j.mtchem.2020.100328>.
- [21] N. Čatić, L. Wells, K.A. Nahas, M. Smith, Q. Jing, U.F. Keyser, J. Cama, S. Kar-Narayan, Aerosol-jet printing facilitates the rapid prototyping of microfluidic devices with versatile geometries and precise channel functionalization, *Appl. Mater. Today* 19 (2020), 100618, <https://doi.org/10.1016/j.apmt.2020.100618>.
- [22] Z. Chen, J.Y. Han, L. Shumate, R. Fedak, D.L. DeVoe, High throughput nanoliposome formation using 3D printed microfluidic flow focusing chips, *Adv. Mater. Technol.* 4 (2019) 1800511, <https://doi.org/10.1002/admt.201800511>.
- [23] A. Patelli, F. Mussano, P. Brun, T. Genova, E. Ambrosi, N. Michieli, G. Mattei, P. Scopece, L. Moroni, Nanoroughness, surface chemistry, and drug delivery control by atmospheric plasma jet on implantable devices, *ACS Appl. Mater. Interfaces* 10 (2018) 39512–39523, <https://doi.org/10.1021/acsami.8b15886>.
- [24] U.M. Dilberoglu, B. Gharehpagh, Y. Yaman, M. Dolen, The role of additive manufacturing in the era of Industry 4.0, *Procedia Manuf.* 11 (2017) 545–554, <https://doi.org/10.1016/j.promfg.2017.07.148>.
- [25] U. Kauscher, J. Penders, A. Nagelkerke, M.N. Holme, V. Nele, L. Massi, S. Gopal, T. E. Whittaker, M.M. Stevens, Gold nanocluster extracellular vesicle supraparticles: Self-assembled nanostructures for three-dimensional uptake visualization, *Langmuir* 36 (2020) 3912–3923, <https://doi.org/10.1021/acs.langmuir.9b03479>.
- [26] Y. Xia, T.D. Nguyen, M. Yang, B. Lee, A. Santos, P. Podsiadlo, Z. Tang, S.C. Glotzer, N.A. Kotov, Self-assembly of self-limiting monodisperse supraparticles from polydisperse nanoparticles, *Nat. Nanotechnol.* 6 (2011) 580–587, <https://doi.org/10.1038/nnano.2011.121>.
- [27] D. Reker, Y. Rybakova, A.R. Kirtane, R. Cao, J.W. Yang, N. Navamajiti, A. Gardner, R.M. Zhang, T. Esfandiary, J. L'Heureux, T. von Erlach, E.M. Smekalova, D. Leboeuf, K. Hess, A. Lopes, J. Rogner, J. Collins, S.M. Tamang, K. Ishida, P. Chamberlain, D. Yun, A. Lytton-Jean, C.K. Soule, J.H. Cheah, A.M. Hayward, R. Langer, G. Traverso, Computationally guided high-throughput design of self-assembling drug nanoparticles, *Nat. Nanotechnol.* 16 (2021) 725–733, <https://doi.org/10.1038/s41565-021-00870-y>.
- [28] Y. Ai, H. Sun, C. Wang, W. Zheng, Q. Han, Q. Liang, Tunable assembly of organic-inorganic molecules into hierarchical superstructures as ligase mimics for enhancing tumor photothermal therapy, *Small* 18 (2022) 2105304, <https://doi.org/10.1002/sml.202105304>.
- [29] Y. Ding, J. Wan, Z. Zhang, F. Wang, J. Guo, C. Wang, Localized Fe(II)-induced cytotoxic reactive oxygen species generating nanosystem for enhanced anticancer therapy, *ACS Appl. Mater. Interfaces* 10 (2018) 4439–4449, <https://doi.org/10.1021/acsami.7b16999>.
- [30] Y. Yu, X. Yang, M. Liu, M. Nishikawa, T. Tei, E. Miyako, Multifunctional cancer phototherapy using fluorophore-functionalized nanodiamond supraparticles, *ACS Appl. Bio Mater.* 2 (2019) 3693–3705, <https://doi.org/10.1021/acsbam.9b00603>.
- [31] D. Maiolo, C. Pigliacelli, P.S. Moreno, M.B. Violatto, L. Talamini, I. Tirrotta, R. Piccirillo, M. Zucchetti, L. Morosi, R. Frapolli, G. Candiani, P. Bigini, P. Metrangola, F.B. Bombelli, Bioreducible hydrophobin-stabilized supraparticles for selective intracellular release, *ACS Nano* 11 (2017) 9413–9423, <https://doi.org/10.1021/acsnano.7b04979>.
- [32] Y. Yu, M. Nishikawa, M. Liu, T. Tei, S.C. Kaul, R. Wadhawa, M. Zhang, J. Takahashi, E. Miyako, Self-assembled nanodiamond supraparticles for anticancer chemotherapy, *Nanoscale* 10 (2018) 8969–8978, <https://doi.org/10.1039/C8NR00641E>.
- [33] S. Paterson, S.A. Thompson, J. Gracie, A.W. Wark, R. de la Rica, Self-assembly of gold supraparticles with crystallographically aligned and strongly coupled nanoparticle building blocks for SERS and photothermal therapy, *Chem. Sci.* 7 (2016) 6232–6237, <https://doi.org/10.1039/C6SC02465C>.
- [34] S. Li, L. Xu, C. Hao, M. Sun, X. Wu, H. Kuang, C. Xu, Porous Cu<sub>2</sub>Co<sub>2</sub>S supraparticles or in vivo telomerase imaging and reactive oxygen species generation, *Angew. Chem. Int. Ed.* 58 (2019) 19067–19072, <https://doi.org/10.1002/anie.201911770>.
- [35] J. Feng, G. Biskos, A. Schmidt-Ott, Toward industrial scale synthesis of ultrapure singlet nanoparticles with controllable sizes in a continuous gas-phase process, *Sci. Rep.* 5 (2015) 15788, <https://doi.org/10.1038/srep15788>.
- [36] J.H. Byeon, J.T. Roberts, Aerosol based fabrication of thiol-capped gold nanoparticles and their application for gene transfection, *Chem. Mater.* 24 (2012) 3544–3549, <https://doi.org/10.1021/cm300601m>.
- [37] H. Ranji-Burachaloo, P.A. Gurr, D.E. Dunstan, G.G. Qiao, Cancer treatment through nanoparticle-facilitated Fenton reaction, *ACS Nano* 12 (2018) 11819–11837, <https://doi.org/10.1021/acsnano.8b07635>.
- [38] J. Chen, S. Pan, J. Zhou, Z. Lin, Y. Qu, A. Glab, Y. Han, J.J. Richardson, F. Caruso, Assembly of bioactive nanoparticles via metal-phenolic complexation, *Adv. Mater.* 34 (2022) 2108624, <https://doi.org/10.1002/adma.202108624>.
- [39] M. Feng, M. Li, R. Dai, S. Xiao, J. Tang, X. Zhang, B. Chen, J. Liu, Multifunctional FeS<sub>2</sub>@SRF@BSA nanoplatform for chemo-combined photothermal enhanced photodynamic/chemodynamic combination therapy, *Biomater. Sci.* 10 (2022) 258–269, <https://doi.org/10.1039/D1BM01597D>.
- [40] F. Zeng, L. Tang, Q. Zhang, C. Shi, Z. Huang, S. Nijati, X. Chen, Z. Zhou, Coordinating the mechanisms of action of ferroptosis and the photothermal effect for cancer theranostics, *Angew. Chem. Int. Ed.* 61 (2022) e202112925.
- [41] P.C. Arroyo, G. David, P.A. Alpert, E.A. Parmentier, M. Ammann, R. Signorelli, Amplification of light within aerosol particles accelerates in-particle photochemistry, *Science* 376 (2022) 293–296, <https://doi.org/10.1126/science.abm7915>.
- [42] C. Yao, H. Qi, X. Jia, Y. Xu, Z. Tong, Z. Gu, D. Yang, A DNA nanocomplex containing cascade DNazymes and promoter-like Zn-Mn-ferrite for combined gene/chemo-dynamic therapy, *Angew. Chem. Int. Ed.* 61 (2022) e202113619.
- [43] A. Curcio, A.V. de Walle, E. Benassai, A. Serrano, N. Luciani, N. Menguy, B. B. Manshian, A. Sargsian, S. Stefaan, A. Espinosa, A. Abou-Hassan, C. Wilhelm, Massive intracellular remodelling of CuS nanomaterials produces nontoxic bioengineered structures with preserved photothermal potential, *ACS Nano* 15 (2021) 9782–9795, <https://doi.org/10.1021/acsnano.1c00567>.
- [44] Y. Wang, Z. Li, Y. Hu, J. Liu, M. Guo, H. Wei, S. Zheng, T. Jiang, X. Sun, Z. Ma, Y. Sun, F. Besenbacher, C. Chen, M. Yu, Photothermal conversion-coordinated Fenton-like and photocatalytic reactions of Cu<sub>2</sub>-Se-Au Janus nanoparticles for tri-combination antitumor therapy, *Biomaterials* 255 (2020), 120167, <https://doi.org/10.1016/j.biomaterials.2020.120167>.
- [45] Y. Liu, J. Wu, Y. Jin, W. Zhen, Y. Wang, J. Liu, L. Jin, S. Zhang, Y. Zhao, S. Song, Y. Yang, H. Zhang, Copper(I) phosphide nanocrystals for in situ self-generation magnetic resonance imaging-guided photothermal-enhanced chemodynamic synergistic therapy resisting deep-seated tumor, *Adv. Funct. Mater.* 29 (2019) 1904678, <https://doi.org/10.1002/adfm.201904678>.
- [46] X. Li, Y. Pan, J. Zhou, G. Yi, C. He, Z. Zhao, Y. Zhang, Hyaluronic Acid-modified manganese dioxide-enveloped hollow copper sulfide nanoparticles as a multifunctional system for the co-delivery of chemotherapeutic drugs and photosensitizers for efficient synergistic antitumor treatments, *J. Colloid Interface Sci.* 605 (2022) 296–310, <https://doi.org/10.1016/j.jcis.2021.07.092>.
- [47] C. Zhang, L. Yan, X. Wang, X. Dong, R. Zhou, Z. Gu, Y. Zhao, Tumor microenvironment-responsive Cu<sub>2</sub>(OH)PO<sub>4</sub> nanocrystals for selective and controllable radiosensitization via the X-ray-triggered Fenton-like reaction, *Nano Lett.* 19 (2019) 1749–1757, <https://doi.org/10.1021/acs.nanolett.8b04763>.
- [48] Y. Zhao, B.-Q. Chen, R.K. Kankala, S.-B. Wang, A.-Z. Chen, Recent advances in combination of copper chalcogenide-based photothermal and reactive oxygen species-related therapies, *ACS Biomater. Sci. Eng.* 6 (9) (2020) 4799–4815.
- [49] Y. Du, C. Yang, F. Li, H. Liao, Z. Chen, P. Lin, N. Wang, Y. Zhou, J.Y. Lee, Q. Ding, D. Ling, Core-shell-satellite nanomaterials as remotely controlled self-fueling Fenton reagents for imaging-guided triple-negative breast cancer-specific therapy, *Small* 16 (2020) 2002537, <https://doi.org/10.1002/sml.202002537>.
- [50] H. Min, Y. Qi, Y. Zhang, X. Han, K. Cheng, Y. Liu, H. Liu, J. Hu, G. Nie, Y. Li, A Graphdiyne oxide-based iron sponge with photothermally enhanced tumor-specific Fenton chemistry, *Adv. Mater.* 32 (2020) 2000038, <https://doi.org/10.1002/adma.202000038>.
- [51] P. An, G. Fan, D. Gu, Z. Gao, A.M.S. Hossain, B. Sun, Photothermal-reinforced and glutathione-triggered in situ cascaded nanocatalytic therapy, *J. Control. Release* 321 (2020) 734–743, <https://doi.org/10.1016/j.jconrel.2020.03.007>.
- [52] S. Wang, T. Hu, G. Wang, Z. Wang, D. Yan, R. Liang, C. Tan, Ultrathin CuFe<sub>2</sub>S<sub>3</sub> nanosheets derived from CuFe-layered double hydroxide as an efficient nanoagent for synergistic chemodynamic and NIR-II photothermal therapy, *Chem. Eng. J.* 419 (2021), 129458, <https://doi.org/10.1016/j.cej.2021.129458>.
- [53] Y. Xu, Y. Guo, C. Zhang, M. Zhan, L. Jia, S. Song, C. Jiang, M. Shen, X. Shi, Fibronectin-coated metal-phenolic networks for cooperative tumor chemo-/chemodynamic/immune therapy via enhanced ferroptosis-mediated immunogenic cell death, *ACS Nano* 16 (2022) 984–996, <https://doi.org/10.1021/acsnano.1c08585>.
- [54] L. An, C. Wang, Q. Tian, C. Tao, F. Xue, S. Yang, X. Zhou, X. Chen, G. Huang, NIR-II laser-mediated photo-Fenton-like reaction via plasmonic Cu<sub>9</sub>S<sub>8</sub> for immunotherapy enhancement, *Nano Today* 43 (2022), 101397, <https://doi.org/10.1016/j.nantod.2022.101397>.
- [55] D.H. Park, Y.H. Joe, J. Hwang, J.H. Byeon, Evaporation-condensation in the presence of unipolar ionic flow for solvent-free production of ultrasmall



- antibacterial particles, *Chem. Eng. J.* 381 (2020), 122639, <https://doi.org/10.1016/j.cej.2019.122639>.
- [56] K. Poudel, S. Park, J. Hwang, S.K. Ku, C.S. Yong, J.O. Kim, J.H. Byeon, Photothermally modulatable and structurally disintegratable sub-8-nm Au<sub>1</sub>Ag<sub>9</sub> embedded nanoblocks for combination cancer therapy produced by plug-in assembly, *ACS Nano* 14 (2020) 11040–11054, <https://doi.org/10.1021/acsnano.9b09731>.
- [57] H. Zhang, H.-J. Chen, X. Du, D. Wen, Photothermal conversion characteristics of gold nanoparticle dispersions, *Solar Energy* 100 (2014) 141–147, <https://doi.org/10.1016/j.solener.2013.12.004>.
- [58] F. Emami, A. Banstola, A. Vatanara, S. Lee, J.O. Kim, J.-H. Jeong, S. Yook, Doxorubicin and anti-PD-L1 antibody conjugated gold nanoparticles for colorectal cancer photochemotherapy, *Mol. Pharmaceutics* 16 (2019) 1184–1199, <https://doi.org/10.1021/acs.molpharmaceut.8b01157>.
- [59] B.K. Poudel, K.-O. Doh, J.H. Byeon, Ag photoionization-induced single-pass assembly of Ag<sub>2</sub>S nanodots in flowing thiol droplets, *Green Chem.* 20 (2018) 978–983, <https://doi.org/10.1039/C7GC03822D>.
- [60] W. Liu, H. Xiang, M. Tan, Q. Chen, Q. Jiang, L. Yang, Y. Cao, Z. Wang, H. Ran, Y. Chen, Nanomedicine enables drug-potency activation with tumor sensitivity and hyperthermia synergy in the second near-infrared biowindow, *ACS Nano* 15 (2021) 6457–6470, <https://doi.org/10.1021/acsnano.0c08848>.
- [61] K. Kwak, J. Choi, J. Lim, J.H. Byeon, Combining plug-in devices for reconfigurable removal of trichloroethylene and heavy metal ion in aqueous solution: Application and biosafety of iron-iron sulfide and its composites, *J. Clean. Prod.* 314 (2021), 128069, <https://doi.org/10.1016/j.jclepro.2021.128069>.
- [62] S. ullah, A. Badshah, F. Ahmed, R. Raza, A.A. Altaf, R. Hussain, Electrodeposited zinc electrodes for high current Zn/AgO bipolar batteries, *Int. J. Electrochem. Sci.* 6 (2011) 3801–3811.
- [63] Z. Li, L. Mi, W. Chen, H. Hou, C. Liu, H. Wang, Z. Zheng, C. Shen, Three-dimensional CuS hierarchical architectures as recyclable catalysts for dye decolorization, *CrystEngComm* 14 (2012) 3965–3971, <https://doi.org/10.1039/C2CE00018K>.
- [64] A. Baral, L. Satish, D.P. Das, H. Sahoo, M.K. Ghosh, Construing the interactions between MnO<sub>2</sub> nanoparticle and bovine serum albumin: Insight into the structure and stability of a protein–nanoparticle complex, *New J. Chem.* 41 (2017) 8130–8139, <https://doi.org/10.1039/C7NJ01227F>.
- [65] X. Liu, B. Li, F. Fu, K. Xu, R. Zou, Q. Wang, B. Zhang, Z. Chen, J. Hu, Facile synthesis of biocompatible cysteine-coated CuS nanoparticles with high photothermal conversion efficiency for cancer therapy, *Dalton Trans.* 43 (2014) 11709–11715, <https://doi.org/10.1039/C4DT00424H>.
- [66] C. Dai, C. Wang, R. Hu, H. Lin, Z. Liu, L. Yu, Y. Chen, Photonic/magnetic hyperthermia-synergistic nanocatalytic cancer therapy enabled by zero-valence iron nanocatalysts, *Biomaterials* 219 (2019) 119374, <https://doi.org/10.1016/j.biomaterials.2019.119374>.
- [67] Q. Chen, X. Shan, S. Shi, C. Jiang, T. Li, S. Wei, X. Zhang, G. Sun, J. Liu, Tumor microenvironment-responsive polydopamine-based core/shell nanoplatfor for synergistic theranostics, *J. Mater. Chem. B* 8 (2020) 4056–4066, <https://doi.org/10.1039/D0TB00248H>.
- [68] Y. Liao, Y. Li, R. Zhao, J. Zhang, L. Zhao, L. Ji, Z. Zhang, X. Liu, G. Qin, X. Zhang, High-entropy-alloy nanoparticles with 21 ultra-mixed elements for efficient photothermal conversion, *Nat. Sci. Rev.* 9 (2022) nwac041, <https://doi.org/10.1093/nsr/nwac041>.
- [69] Y. Li, Y. Liao, J. Zhang, E. Huang, L. Ji, Z. Zhang, R. Zhao, Z. Zhang, B. Yang, Y. Zhang, B. Xu, G. Qin, X. Zhang, High-entropy-alloy nanoparticles with enhanced interband transitions for efficient photothermal conversion, *Angew. Chem. Int. Ed.* 60 (2021) 27113–27118, <https://doi.org/10.1002/anie.202112520>.
- [70] Y. Xin, K. Yu, L. Zhang, Y. Yang, H. Yuan, H. Li, L. Wang, J. Zeng, Copper-based plasmonic catalysts: Recent advances and future perspectives, *Adv. Mater.* 33 (2021) 2008145, <https://doi.org/10.1002/adma.202008145>.
- [71] Z. Wang, P. Huang, O. Jacobson, Z. Wang, Y. Liu, L. Lin, J. Lin, N. Lu, H. Zhang, R. Tian, G. Niu, G. Liu, X. Chen, Biomimetic-inspired synthesis of copper sulfide–ferritin nanocages as cancer theranostics, *ACS Nano* 10 (2016) 3453–3460, <https://doi.org/10.1021/acsnano.5b07521>.
- [72] T. Dai, Y. Wan, R. Tian, S. Wang, T. Han, G. Wang, In situ cation exchange generated ZnS–Ag<sub>2</sub>S nanoparticles for photothermal detection of transcription factor, *ACS Appl. Bio Mater.* 3 (2020) 3260–3267, <https://doi.org/10.1021/acsaabm.0c00232>.
- [73] J.-S. Baek, C.-W. Cho., Comparison of solid lipid nanoparticles for encapsulating paclitaxel or docetaxel, *J. Pharm. Investig.* 45 (2015) 625–631, <https://doi.org/10.1007/s40005-015-0182-3>.
- [74] Y.-H. Lai, C.-S. Chiang, C.-H. Hsu, H.-W. Cheng, S.-Y. Chen, Development and characterization of a fucoidan-based drug delivery system by using hydrophilic anticancer polysaccharides to simultaneously deliver hydrophobic anticancer drugs, *Biomolecules* 10 (7) (2020) 970.
- [75] A. Retnakumari, S. Setua, D. Menon, P. Ravindran, H. Muhammed, T. Pradeep, S. Nair, M. Koyakutty, Molecular-receptor-specific, non-toxic, near-infrared-emitting Au cluster-protein nanoconjugates for targeted cancer imaging, *Nanotechnology* 21 (2010) 055103, <https://doi.org/10.1088/0957-4484/21/5/055103>.
- [76] X. Li, R. Luo, X. Liang, Q. Wu, C. Gong, Recent advances in enhancing reactive oxygen species based chemodynamic therapy, *Chin. Chem. Lett.* 33 (2022) 2213–2230, <https://doi.org/10.1016/j.ccl.2021.11.048>.
- [77] J.W. Hodge, C.T. Garnett, B. Farsaci, C. Palena, K.-Y. Tsang, S. Ferrone, S. R. Gameiro, Chemotherapy-induced immunogenic modulation of tumor cells enhances killing by cytotoxic T lymphocytes and is distinct from immunogenic cell death, *Int. J. Cancer* 133 (2013) 624–636, <https://doi.org/10.1002/ijc.28070>.
- [78] C.T. Garnett, J. Schlom, J.W. Hodge, Combination of docetaxel and recombinant vaccine enhances T-cell responses and antitumor activity: Effects of docetaxel on immune enhancement, *Clin. Cancer Res.* 14 (2008) 3536–3544, <https://doi.org/10.1158/1078-0432.CCR-07-4025>.
- [79] Y. Liu, H. Li, S. Li, X. Zhang, J. Xiong, F. Jiang, Y. Liu, P. Jiang, Chiral Cu<sub>2</sub>xSe nanoparticles for enhanced synergistic cancer chemodynamic/photothermal therapy in the second near-infrared biowindow, *ACS Appl. Mater. Interfaces* 13 (2021) 60933–60944, <https://doi.org/10.1021/acsaami.1c20486>.
- [80] L. Tan, J. Wan, W. Guo, C. Ou, T. Liu, C. Fu, Q. Zhang, X. Ren, X.-J. Liang, J. Ren, L. Li, X. Meng, Renal-clearable quaternary chalcogenide nanocrystal for photoacoustic/magnetic resonance imaging guided tumor photothermal therapy, *Biomaterials* 159 (2018) 108–118, <https://doi.org/10.1016/j.biomaterials.2018.01.003>.
- [81] Q. Chen, Y. Luo, W. Du, Z. Liu, S. Zhang, J. Yang, H. Yao, T. Liu, M. Ma, H. Chen, Clearable theranostic platform with a pH-independent chemodynamic therapy enhancement strategy for synergetic photothermal tumor therapy, *ACS Appl. Mater. Interfaces* 11 (2019) 18133–18144, <https://doi.org/10.1021/acsaami.9b02905>.